Effect of periodic unsteadiness on heat transfer in a turbulent boundary layer downstream of a cylinder-wall junction

Q. Xie and D. Wroblewski
Department of Aerospace and Mechanical Engineering, Boston University, Boston, MA

The heat transport and wall heat transfer in a turbulent boundary layer downstream of a cylinder-wall junction has been investigated experimentally. The heat transfer effect of local periodic, large-scale unsteadiness, as a result of vortex shedding from the cylinder, was examined using a conditional data-sampling and analysis technique that separated the large-scale periodic motion from the background turbulence. Detailed measurements of temperature and velocity were obtained using a cold wire and a custom-designed heat-flux probe. Thin-film, heat-flux surface sensors were used to obtain the time-resolved wall heat flux. Experiments were conducted approximately 5 diameters downstream of the leading edge of the cylinder, at $Re_D = 36{,}000$ and $Re_L = 970{,}000$. The boundary-layer transport and wall heat transfer were affected by the presence of large-scale periodic unsteadiness arising from vortex shedding in a region spanning approximately 2 diameters on either side of the cylinder. Large-scale fluctuations of the time-resolved wall-Stanton number were caused by the thinning and thickening of the near-wall thermal layer by periodic fluctuations in the vertical component of velocity. © *1997 by Elsevier Science Inc.*

Keywords: junction flow; unsteady convection; turbulent heat flux measurements; conditional sampling

Introduction

When a boundary layer growing along a flat plate confronts a protruding obstacle, such as a bluff body or streamlined body, a complex three-dimensional (3-D) flow field forms around and behind the body. Examples of such flow in fluid and heat transfer engineering are many and varied, such as: wing/body junction on aircraft; base blows near buildings and support poles; endwall junction of gas turbine blades; base flows of a plate fin heat exchanger; and the junctions of circuit boards and protruding electronic components. Figure 1 shows the schematic of such a junction boundary-layer flow with a cylinder as the obstacle. The mean shear within the bottom of the approaching boundary layer at the leading edge of the obstacle is skewed by the adverse pressure gradient. The boundary layer separates and rolls up to form a primary vortex along with a smaller counter-rotating vortex at the leading edge. The fluid in the vicinity and downstream of the junction wraps the vortex system around the obstacle, resulting in two streamwise vortex legs, called a horseshoe or necklace vortex. The boundary layer and free stream above the junction separate around the trailing-edge of the body and generate a turbulent wake region behind the body. Periodic shedding of Kàrmàn vortices from bluff obstacles can further complicate the flow field downstream of the body. There has been a considerable amount of research aimed at understanding the fluid dynamics behavior of the complex bluff body–wall junction flow. However, the convective heat transfer in the region downstream, which is controlled by the complex interactions between the turbulent boundary layer, horseshoe vortex trailing legs, the obstacle wake, and the vortex shedding, is not as well characterized.

Baker (1979, 1980) and Goldstein and Karni (1984) have investigated the leading-edge region and characterized the motion of the horseshoe vortex system. Hunt et al. (1978) visualized flow around the surface-mounted obstacles. Oertel (1990) and Norberg (1994) summarized the behavior of the vortex shedding and wake behind blunt bodies. Extensive mean velocity and turbulent measurements have been made by Shabaka et al., (1985), Sparrow (1984), Pierce and Harsh (1988), and others.

Praisner et al. (1996) mapped the wall heat transfer characteristics of the stagnation point region, using a liquid crystal technique, and attributed the large-scale temporal variations to random eruptions of near-wall fluid due to interaction between the primary and secondary vortices of the horseshoe vortex system. Fisher and Eibeck (1990) measured mean heat transfer rates downstream of a circular cylinder and a tapered cylinder junction. The results showed up to 50% enhancement in Stanton number over undisturbed flat-plate values attributed to the present of the horseshoe vortex. Wroblewski and Eibeck (1992) measured the turbulent velocity and temperature field in a heated boundary layer downstream of a tapered cylinder and a wall junction. The results show that the periodic vortex shedding greatly increased the turbulent heat transport in the flow field. Tyszka and Wroblewski (1996) studied heat transfer in a turbu-

---

Address reprint requests to Dr. D. Wroblewski, Department of Aerospace and Mechanical Engineering, Boston University, Boston, MA 02155, USA.

Received 10 March 1966; accepted 15 October 1996

Int. J. Heat and Fluid Flow 18: 107–115, 1997
© 1997 by Elsevier Science Inc.
655 Avenue of the Americas, New York, NY 10010

0142-727X/97/$17.00
PII S0142-727X(96)00143-7

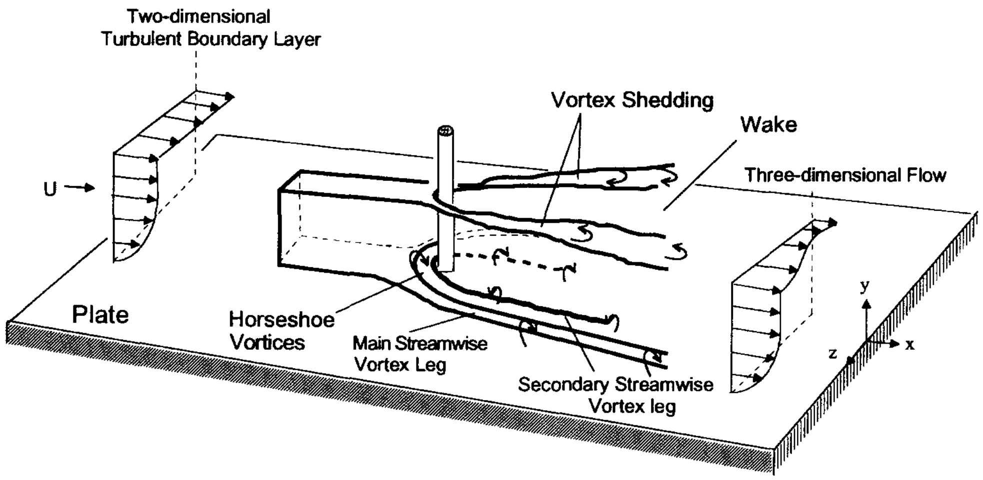

Figure 1 Schematic of junction boundary-layer flow

lent boundary layer downstream of a truly streamlined body junction. The study did not find the significant endwall heat transfer enhancement downstream of the body that was observed in previous studies with bluff bodies. This may have been due to the fact that there was no strong wake region or strong horseshoe vortex present in the near-wall region behind the streamlined body.

Wroblewski (1996) experimentally studied the effects of large-scale periodic unsteadiness, attributable to vortex shedding, on heat transport downstream of a streamlined cylinder. Detailed turbulence measurements were made in the flow field using triple-wire heat-flux probes. Effects due to flow unsteadiness were separated from those due to background turbulence using a triple decomposition and conditional sampling technique. The results revealed that up to 30% of the total vertical component and 54% of the spanwise component of the Reynolds heat flux were caused by the presence of periodic unsteadiness, which distorted the thermal boundary layer more than the outer motions in an ordinary turbulent boundary layer.

Increasing attention has been focused on the study of turbulent flows superimposed with global periodic unsteadiness (i.e., oscillating or pulsatile modulations of the flow). However, the unsteadiness observed in the junction boundary layer is a local phenomenon, and although its influence on boundary-layer

Notation

c_p	specific heat, (J/kg°C)
D	diameter of the cylinder models, m
E_m	microphone voltage output, V
E_{vv}	power spectrum of vertical velocity component, (m^2/s)
$E_{\theta\theta}$	power spectrum of temperature, $(K^2 \cdot s)$
E_{qq}	power spectrum of wall heat flux $(W^2 \cdot s/m^4)$
f	frequency, Hz
L	distance from boundary-layer trip to the cylinder leading edge, m
N	total number of periodic event cycles
q_w	instantaneous wall heat flux, (W/m^2)
$\bar{q}_w$	long-time mean wall hat flux, (W/m^2)
$\tilde{q}_w$	ensemble-averaged mean wall heat flux, (W/m^2)
Re_D	Reynolds number based on the cylinder diameter, $\mathrm{Re}_D \equiv U_\infty D/\nu$
Re_L	Reynolds number based on the characteristic length L, $\mathrm{Re}_L \equiv U_\infty \mathrm{L}/\nu$
S	Strouhal number, $\mathrm{S} \equiv fD/U_\infty$
St	long-time mean Stanton number, $\mathrm{St} \equiv \bar{q}_w/[\rho C_p U_\infty(T_w - T_\infty)]$
$\tilde{\mathrm{St}}$	ensemble-averaged mean Stanton number, $\tilde{\mathrm{St}} \equiv \tilde{q}_w/[\rho C_p U_\infty(T_w - T_\infty)]$
t_i	time mark for the ith periodic event cycle, s
T	period of the unsteady events, s
T_∞	free-stream temperature, °C
$T_{w,2d}$	wall temperature without cylinder installed, °C
U_i	instantaneous velocity component, (m/s)
$\bar{u}$	long-time mean streamwise velocity component, (m/s)
U_0	velocity at entrance of the test section, (m/s)
U_∞	local free-stream velocity, (m/s)
$\overline{u_i'\theta'}$	turbulence contribution to the Reynolds heat flux, (m°C/s)
$\overline{\tilde{u}_i\tilde{\theta}}$	unsteadiness contribution to the Reynolds heat flux, (m°C/s)
$\tilde{v}$	ensemble-averaged mean vertical velocity component, (m/s)
v	total fluctuation of vertical velocity component, (m/s)
w	total fluctuation of spanwise velocity component, (m/s)
x	streamwise coordinate, m
y	vertical coordinate, m
y^+	nondimensional vertical inner-layer distance $y^+ \equiv u_\tau y/\nu$
z	spanwise coordinate, m
Greek	
Θ	instantaneous temperature, °C
$\bar{\theta}, \tilde{\theta}$	long-time and ensemble-averaged mean temperature, °C
θ	total fluctuation of temperature, °C
ν	kinematic viscosity, $\nu \equiv \mu/\rho$ (m^2/s)
ρ	density of air, (kg/m^3)
τ	phase time relative to time marks, s

transport has been documented, its role in the enhanced downstream wall heat transfer rates is not clear. The objective of this research was to study the effect of local, large-scale periodic unsteadiness on wall heat transfer. Measurements of time-resolved wall heat fluxes and turbulent transport within the flow field were obtained so that the thermal boundary-layer dynamics could be correlated with the unsteady heat transfer behavior. Such correlations were obtained by means of conditional sampling and triple decomposition combined with ensemble averaging.

Experimental arrangement

Experimental facility

The research was conducted in an open-circuit wind tunnel located in the Fluid Mechanics Laboratory at the Department of Aerospace and Mechanical Engineering of Boston University. The working section of this tunnel was 3.05-m (10 ft) long with a cross section of 914-mm × 305-mm (36 × 12 in). Maximum flow speed was 25 m/s. The constant cross-sectional area of the working section resulted in a slightly favorable pressure gradient due to the growth of the wall boundary layers; the velocity at the test measurement plane was approximately 5% higher than the velocity at the entrance of the test section. The momentum-boundary layer was tripped by a 2-mm-high and 10-mm-wide balsa wood strip at the entrance of the test section and then developed over an unheated floor. A circular cylinder of diameter 57 mm (2.25 in), spanning the height of the tunnel, was placed in the middle of the test section downstream of the developing section. Figure 2 is the schematic of the test section setup.

A separate floor section downstream of the cylinder consisted of three surface modules, each 953-mm (37.5 in) wide and 457-mm (18 in) long. Two types of surface modules were used. First, constant heat flux surfaces with embedded thermocouples were used to obtain time-mean wall heat transfer coefficients and for thermal boundary-layer transport measurements. Heat transfer coefficients were obtained from the heater input power, corrected for radiation and conduction losses, and surface temperatures measured with the embedded thermocouples. Velocities and temperatures were obtained by traversing the cold wire and heat-flux probes through the flow field. Second, unheated surfaces with flush-mounted, heated, thin-film heat-flux sensors were used to obtain time-resolved wall heat transfer coefficients. This type of technique; i.e., an unheated surface with small patches of local heating, yielded adiabatic heat transfer coefficients that isolated the local hydrodynamic effects on heat transfer from the upstream heating effects.

The heated surface modules were fabricated from a thin metal film sheet that was similar to those used by Baughn et al. (1985), who employed a gold-coated plastic sheet to generate uniform wall heat flux. The metal film sheet, manufactured by Cortlaulds Performance Films, consisted of a 4000-Å thick layer of copper and 400-Å thick layer of nickel sputtered onto a 0.18-mm thick polyester substrate. Each heater element, 762-mm (30 in) wide and 457-mm (18 in) long, was attached to a 953-mm (37.5 in) × 457-mm (18 in) × 5-mm (0.19 in) thick Lexan sheet to provide a flat and rigid backing. The back of the lexan was insulated with 25-mm thick foam insulation sandwiched between two 1.5-mm thick rigid plywood plates. A smooth upper heating surface was obtained by bonding a 0.1-mm thick plastic sheet to the top of the heater element, using a layer of 0.3-mm thick doubled-sided adhesive liner. Type-T thermocouples were attached underneath the surface of the polyester substrate sheet of the heater element, with thermoconductive epoxy used to ensure good thermal contact.

Mean and fluctuating measurements of temperature and velocity were obtained for the two-dimensional (2-D) boundary layer (i.e., no obstacle presented) to qualify the wind-tunnel facility and measurement techniques. The free-stream turbulent intensity was found to be less than 0.2% at an entrance velocity of $U_0 = 25$ m/s. The boundary-layer momentum thickness and velocity log-region profile measured by a single hot wire agreed with accepted 2-D boundary-layer results within 5% (see Xie 1996).

Experiments were conducted at a Reynolds number of $\mathrm{Re}_D = U_\infty D/\nu = 36{,}000$ (U_∞ is the local free-stream velocity, and D is the cylinder diameter) and $\mathrm{Re}_L = U_\infty L/\nu = 970{,}000$ (L is the distance from the boundary-layer trip to the cylinder leading edge). The ratio of 2-D boundary-layer thickness to cylinder diameter was 0.57. Data were taken on only one side of the measurement plane, assuming the mean characteristics of the flow field behind the cylinder were symmetric. Note that the boundary-layer transport measurements were obtained for negative values of z/D, while the surface sensor measurements were obtained for positive values of z/D.

Measurement probes

A triple-wire probe, custom manufactured by TSI Inc., was used to obtain the Reynolds heat fluxes and stresses within the flows under consideration. The probe consisted of two hot wires arranged in a vertical X-wire configuration, to measure U and V components of velocity and a cold wire located in front of and in a plane perpendicular to the X-wire to measure temperature. The X-wire consisted of 2.5-μm diameter tungsten sensors, with 23-μm diameter copper plating along the ends. The total length of the hot wires was 1.27 mm and the active length of the sensors was 0.6 mm. The cold wire was a 0.8-mm long and a 1.3-μm diameter platinum wire. The X-wires were operated with a TSI IFA-100 constant temperature anemometer system, while the

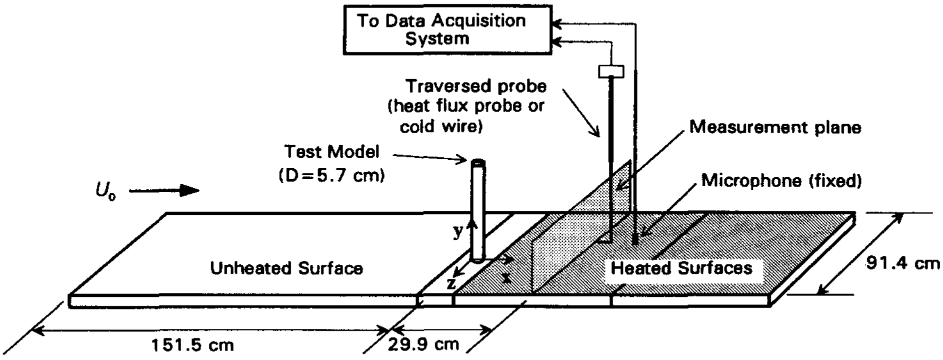

Figure 2 Schematic of test section used for transport measurements

cold-wire was operated with the TSI Temperature Module 145 constant current anemometer.

A single cold wire (TSI model 1218-P0.5), using the same sensor as the heat-flux probe, was also used for instantaneous temperature measurement in the turbulent flow field, because it could reach positions closer to the wall than the heat-flux probes (typically 0.5 mm).

The heat-flux probe and the single cold-wire probe were calibrated in a laminar jet, with controls for varying the jet velocity, jet temperature, pitch, and yaw angle of the probe. The procedures and calibration equations for the hot and cold wires are discussed in more detailed in Xie (1996).

Thin-film surface heat-flux sensor

Thin-film surface sensors, similar to those employed by Swisher and Diller (1992), were used to measure time-resolved wall heat flux for selected positions along the wall. These devices, pictured in Figure 3, consisted of a 0.18-mm thick polyester sheet coated with a thin gold film, attached to a thermoresistive substrate (foam insulation inside a 12.7-mm diameter plastic tube). The gold-coated polyester sheet is similar to the heating element used for the heated-surface module. The coating of gold was thin enough to be somewhat transparent and to act as a resistance heating element. These thin-film surface sensors, similar to standard hot-film sensors, were operated with a constant temperature anemometer that maintained the sensor surface at a constant temperature. The heat flux was determined by the electrical voltage across the sensor, provided by the anemometer output, and the sensor resistance, which was set on the anemometer.

The surface sensors were calibrated using three different tests. First, the temperature coefficient of resistance was determined by immersing a patch of the gold film in a temperature-controlled water bath. A value of 0.0012°C^{-1} was determined; this agreed well with measurements by Baughn et al. (1985) on similar gold films.

Second, the sensors were installed and operated in the wind tunnel, without the cylinder, to determine the mean heat transfer characteristics. For this situation, the expected heat transfer coefficient from an isothermal patch on an otherwise adiabatic wall was predicted from a numerical solution of the 3-D convection–diffusion equation. Because the thin thermal boundary layer does not grow into the log layer, the equation needed to be solved only out to a value of $y^+ = 30$. The "known" velocity field was determined from the local shear stress and the universal profile for a two-dimensional (2-D) turbulent boundary layer. The eddy-diffusivity was predicted using a mixing length model with a Van Driest correction and a conduction model for the turbulent Prandtl number (Kays and Crawford 1993). It should be noted that the majority of the thermal boundary layer is within the viscous sublayer, so the prediction of the heat transfer coefficient is dependent mostly on the value of the shear stress and only mildly on the assumptions of the buffer-layer behavior. The actual measured values of the heat transfer coefficient were correlated with the predicted values to generate a linear calibration curve. Results indicated that errors due to conduction and radiation were approximately 40%.

The above calibration was for the mean values only. The unsteady response of the surface sensors is very difficult to calibrate, because there is no device that can supply a known fluctuating convective heat flux. A square-wave heat input test, a standard feature of commercial CTA systems, was used to estimate the frequency response of the sensor and anemometer combination. The response was better than 1500 Hz, which was more than adequate for the relatively low-frequency structures that were of interest in the present study. Although the square-wave test does not provide a rigorous unsteady calibration for this type of sensor, the measured fluctuations in the heat flux should be qualitatively correct, within a frequency band determined by the measured square-wave response.

Reference Probe and data acquisition

A 12-mm diameter condenser microphone connected to an audio-quality tape deck, was used to detect the large-scale, unsteady events, by sensing the associated pressure fluctuations. The output voltage signal, amplified and filtered at 500 Hz was used as a reference signal for conditional sampling and ensemble averaging. Use of a reference probe provided the ability to correlate data at different locations and from different probes, without the need to acquire the data simultaneously.

A 80486-based computer with an A/D interface board was used for sampling output signals from the heat-flux probe, cold-wire sensor, surface sensor and microphone. The A/D board featured four simultaneous-sample-and-hold channels. All test data was obtained at a sampling frequency of 4000 Hz and a low-pass filter frequency of 2000 Hz, except the data from the microphone.

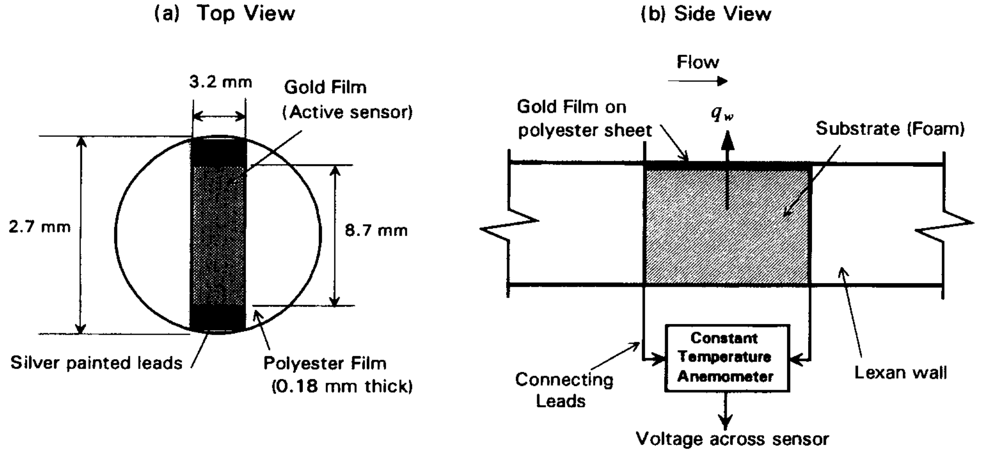

Figure 3 Schematic of thin-film heat-flux surface sensor

Data analysis technique

Triple decomposition

The triple decomposition method was used to analyze this complex turbulent flow superimposed with large-scale periodic unsteadiness. The velocities and temperature were decomposed into three components, rather than the usual two components for the classical Reynolds decomposition. Using this method, for example, the instantaneous temperature, $\Theta(t)$ is expressed as

$$\Theta(t) = \bar{\theta} + \tilde{\theta}(\tau) + \theta'(t_i,\tau) \tag{1}$$

where $\bar{\theta}$ is the long-time mean temperature; $\tilde{\theta}(\tau)$ is the fluctuation about the mean due to the periodic unsteadiness, as a function of τ (the time relative to some reference point in the periodic cycle); and $\theta'(t_i,\tau)$ is the turbulent fluctuation about the periodic mean at the specific time $(t_i + \tau)$. The total fluctuation about the long-time mean is $\theta(t_i,\tau) = \tilde{\theta}(\tau) + \theta'(t_i,\tau)$.

While the long-time mean results in a single value, the periodic mean, calculated from ensemble-averaging data of a number of cycles, results in a function of τ representing an average or typical cycle of the event. For example, the periodic mean temperature is calculated from

$$\tilde{\theta}(\tau) = \frac{1}{N}\sum_{i=1}^{N} \theta(t_i,\tau) \tag{2}$$

where N is the total number of cycles.

A modified form of the Reynolds-averaged equations can be derived with the triple decomposition method. For example, the energy equation becomes

$$\frac{\partial\bar{\theta}}{\partial t} + \bar{U}_i\frac{\partial\bar{\theta}}{\partial x_i} = \kappa\frac{\partial^2\bar{\theta}}{\partial x_i\partial x_i} - \frac{\partial\overline{\theta' u_i'}}{\partial x_i} - \frac{\partial\overline{\tilde{\theta}\tilde{u}_i}}{\partial x_i} \tag{3}$$

where $\overline{\tilde{u}_i\tilde{\theta}}$ represent the contributions to the Reynolds heat fluxes due to the periodic unsteadiness, and $\overline{u_i'\theta'}$ are the contributions from the background turbulent fluctuations. Similar equations can be developed for the momentum field.

Conditional sampling

A conditional-sampling technique was employed to separate the large-scale motions from the background turbulence. During the experiments, the microphone was located at a fixed point ($x/D = 5.94$, $y/D = 0.11$, $z/D = 0.67$) just downstream of the measurement plane. Because the time period between each vortex-shedding event was variable, the pressure fluctuations sensed by the microphone were used to identify the onset of an unsteady event. Temperature, velocities, and wall heat flux at different locations were then ensemble-averaged based on the reference time provided by the microphone. In this manner, it was possible to extract the effect of the large-scale motions on heat transport and wall heat transfer from that of the background turbulence.

Figure 4 shows typical instantaneous microphone voltage output at the fixed reference location with an without the cylinder installed upstream. Comparing these two flow cases, the large and steep fluctuation in pressure sensed by the microphone with the cylinder indicated the passing of an unsteady event. The spectra of this unsteadiness also exhibited distinct periodic features at a frequency that matched the expected vortex-shedding frequency of approximately 32 Hz. A smaller peak is also observed at the first harmonic frequency, 64 Hz. The large-scale peaks in the microphone output signal were used to identify the occurrence of the unsteadiness and to set the reference time mark for ensemble averaging.

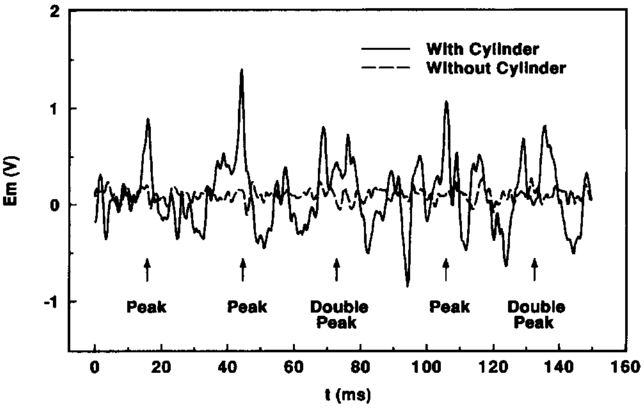

Figure 4 Instantaneous microphone voltage output E_m with and without cylinder

The event detection and ensemble averaging procedures were as follows. First, the microphone output was sampled simultaneously with the heat-flux probe, cold-wire probe, or thin-film surface sensor outputs. The microphone position was fixed for all measurements at a location near the wall and at a spanwise location at which the pressure peaks were found to be the largest. Second, potential events were identified by local peaks of the pressure signal which were higher than specific threshold value. A sensitivity analysis revealed that the number of detected events was approximately constant within a broad range of threshhold values. A value of 0.6 volts, approximately in the center of the range, was chosen. Two standards were used to finally resolve the reference time mark for a passing unsteady event: (1) if the interval time between two consecutive pressure peaks was larger than a given threshold interval (usually 65%T, where T is the event period based on the average frequency), the position of the pressure peak was used as a reference point indicating the presence of an unsteady event; and (2) if the interval time between two consecutive pressure peaks was smaller than the given threshold interval, which was an indication of a double peak, as seen in Figure 4, the reference point was chosen as the point where the correlation coefficient between the pressure signal and a cosine wave, with a frequency equal to the shedding frequency, was maximum. All the reference points identified from the microphone output were then saved for ensemble averaging. Third, the velocities, temperatures, and wall heat fluxes were ensemble averaged over all detected events. The averaging period began one full event period ahead of the reference marks set by the microphone data to account for the time lag caused by streamwise distance between microphone and the probes. Contributions from background turbulence were obtained by subtracting long-time mean and periodic mean from the instantaneous values.

Results

Time-mean results

Iso contours of the long-time mean streamwise velocity and temperature are presented in Figures 5 and 6. The mean velocity is normalized by the local free-stream velocity U_∞, and the temperature is normalized by free-stream temperature T_∞, and the wall temperature measured at the same streamwise location without the cylinder present $T_{w,2d}$. The velocity contours are nearly horizontal in the region far from the centerline ($z/D <$

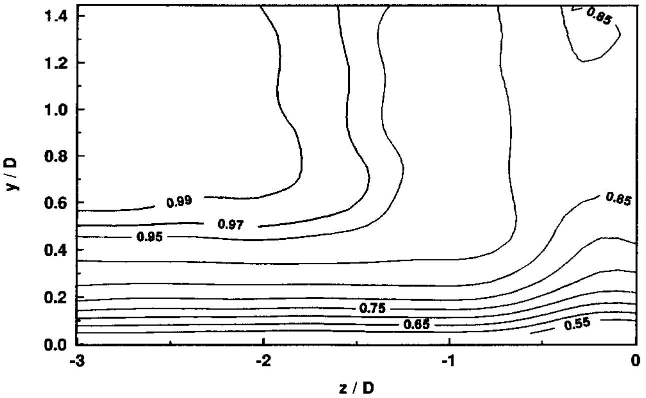

Figure 5 Isocontours of long-time mean streamwise velocity, $\bar{u}/U_\infty$, at $x/D = 5.2$

-2), indicating an undisturbed 2-D boundary layer. The contour lines turn upward in the region near the centerline ($z/D > -1$), where the obstacle wake creates a large momentum deficit.

Similar to streamwise velocity contour in the outer spanwise region, the temperature profiles are approaching 2-D behavior in that region ($z/D < -2$). The temperature contours dip toward the wall for $z/D > -2$, indicating that the temperature near the wall is decreasing. This suggests that the near-wall thermal layer is thinning. Toward the centerline, the temperature contour lines curve upward, far away from the wall, indicating that the overall thermal boundary layer is thickening.

These data suggest three main spanwise zones, similar to those defined by Wroblewski (1996) for the streamlined cylinder case: (1) a wake zone, close to the centerline, where the mean behavior seems to be governed by the obstacle wake turbulence; (2) an outer zone $z/D < -2$, where behavior is governed by 2-D boundary-layer mechanisms; and (3) an unsteady zone, where the 3-D nature of the flow is most evident and where the unsteady effects are expected to be most dominant (Wroblewski 1996). This latter effect will be confirmed with the ensemble-averaged data.

The spanwise distribution of the ratio of mean Stanton number with the cylinder to the Stanton number without the cylinder is shown in Figure 7 for both sides downstream of the cylinder. The peak Stanton number enhancement, approximately 23%, occurs between $z/D = -0.5$ and -1.0 in the unsteady region. This is consistent with mean temperature data, which suggests that the thinnest thermal boundary layer near the wall is near $z/D = -0.5$. It is interesting to note that the maximum value does not occur directly at the centerline position, which is also consistent with the mean temperature contours, which show a thicker thermal layer in the wake region. In the outer region, the ratio approaches a level value close to unity, confirming a return to 2-D characteristics. The overall behavior of mean wall heat transfer is consistent with the data of Fisher and Eibeck (1990).

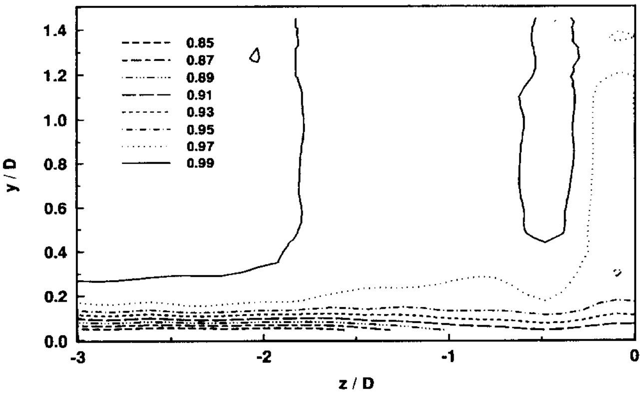

Figure 6 Isocontours of long-time mean temperature, $(\bar{\theta} - T_{w,2d})/(T_\infty - T_{w,2d})$ at $x/D = 5.2$

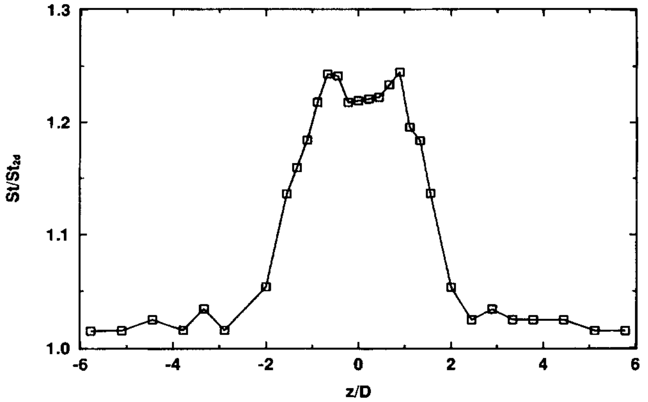

Figure 7 Mean Stanton number ratio, St/St_{2d}, at $x/D = 6.2$

Instantaneous results

Figure 8 shows typical instantaneous fluctuations of vertical velocity v and temperature θ at $x/D = 4.77$, $y/D = 0.042$, $z/D = -1.22$, which is located within the unsteady region and the corresponding microphone voltage output at the reference point. The steep drop in temperature, followed by a period of relatively low constant temperature, which is approximately the same as the measured free-stream temperature, denotes the passing of the interface between the warm fluid in the thermal boundary layer and the cold free-stream fluid. Note that the fluctuations in the vertical velocity correlate well with the temperature behavior, with increasing θ associated with positive v (upwash), and decreasing θ with negative v (downwash). This suggests that the periodic features in the temperature signal are due to large-scale thinning and thickening of the thermal boundary layer.

To confirm that the vortex shedding is the main source of unsteadiness in the flow field, power spectra of θ and v were obtained at several positions. Figures 9 and 10 show results at $y/D = 0.042$ for spanwise locations of $z/D = -0.09, -0.44, -1.22$, and $z/D = -2.80$, located, respectively, in the wake region, unsteady region, unsteady region, and outer region.

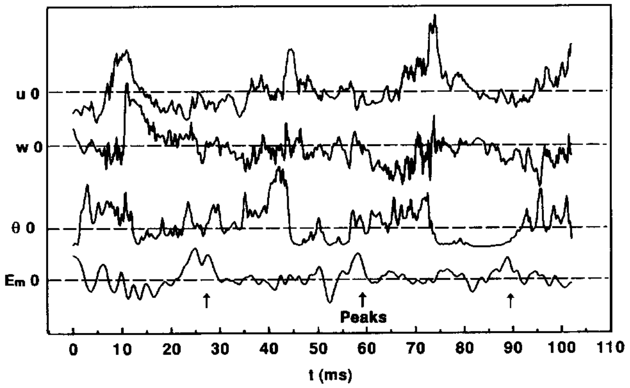

Figure 8 Instantaneous fluctuations of vertical velocity, v, temperature θ, and microphone voltage E_m

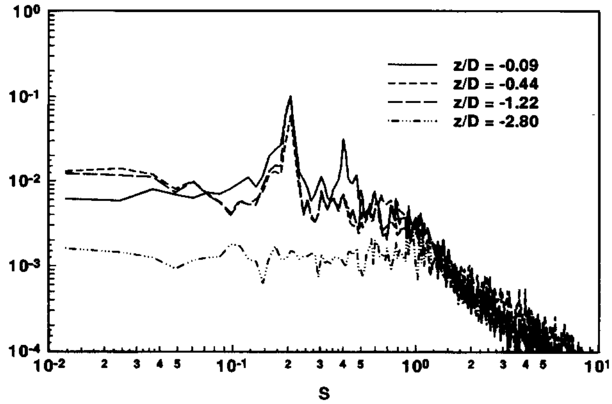

Figure 9 Power spectra of vertical velocity E_{vv} at different spanwise locations $x/D = 5.2$, $y/D = 0.042$ ($S = fD/U_\infty$)

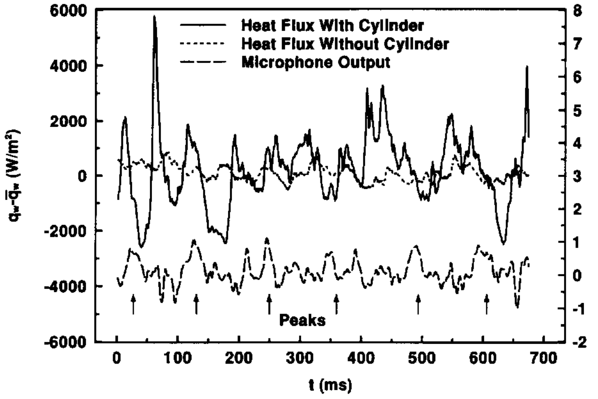

Figure 11 Instantaneous fluctuations in wall heat flux $q_w - \bar{q}_w$, at $x/D = 5.2$, $z/D = 0.44$, and microphone voltage output E_m

In the unsteady region, the spectra of θ and v reveal a dominant peak at a frequency corresponding to a Strouhal number of $S = 0.2$, ($S = fD/U_\infty$), which matches the expected vortex-shedding frequency. It is interesting to note that the spectra of v in the wake region, such as plotted in Figure 9, indicate a second peak near the first harmonic frequency $S = 0.4$. This evidence may suggest that the probe senses the vortex shedding from both sides of the cylinder, because it is located directly behind the cylinder. Spectrum at the point in the outer region has no dominant frequency that indicates that the flow returns to its undisturbed nature.

To examine whether the wall heat transfer is affected by this periodic unsteadiness, the wall heat flux fluctuations measured by the surface sensor were compared with and without the cylinder. Figure 11 shows the simultaneous fluctuations of wall heat flux at $z/D = 0.44$ and the corresponding pressure fluctuation measured at the reference point. The negative values indicate instantaneous wall heat fluxes less than the long-time mean value. Similar to the flow-field results, periodic features can also observed in the wall heat flux data.

Figure 12 presents the power spectrum of wall heat fluxes at three different spanwise locations. The spectra from the unsteady region ($z/D = 0.44$ and 1.44) reveal a peak at the expected vortex shedding frequency $S = 0.2$, indicating that the instantaneous wall heat transfer fluctuations at these spanwise locations could be attributed to vortex shedding unsteadiness. At $z/D = 0.11$, the spectrum does not show a distinct peak at $S = 0.2$, but does reveal a peak near the first harmonic $S = 0.4$. This suggests that the wall heat transfer in the region close to the centerline is affected by the interaction of the wake and vortex shedding from both sides of the cylinder.

Ensemble-averaged results

Figure 13 presents ensemble-averaged wall heat flux $\tilde{St}$ at $z/D = 0.44$, and vertical velocity, $\tilde{v}$, and temperature, $\tilde{\theta}$ at $z/D = -0.44$ and $y/D = 0.042$, which was directly above the surface sensor. The data are normalized with the corresponding total rms values, $\sqrt{\overline{\theta^2}}$ and $\sqrt{\overline{v^2}}$, which include contributions from both the unsteadiness and the background turbulence. The negative $\tilde{St}$ values indicate that the ensemble-averaged mean Stanton number is less than the long-time mean value. The heat flux is characterized by a decrease and then an increase to a peak value, followed by a second drop to a plateau value. This is accompanied by an analogous, but opposite, trend in temperature and vertical velocity field. It is noticed that the velocity and temperature have the same fluctuation pattern but with a small time delay. As the flow moves toward the wall, the temperature starts to drop, resulting in an increase of wall heat transfer rate to its maximum value, and then remains at a flat level, resulting in a decrease of wall heat transfer from its peak value. This behavior indicates that the large-scale unsteadiness affected wall heat transfer mainly through the thinning (decreasing temperature) and thickening (increase temperature) of the thermal boundary layer, an idea discussed further below.

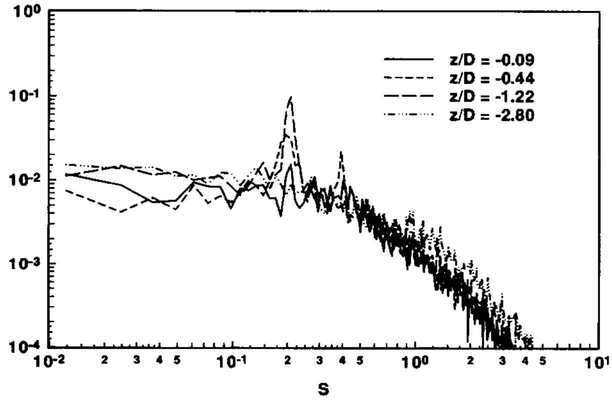

Figure 10 Power spectra of temperature $E_{\theta\theta}$ at different spanwise locations, $x/D = 5.2$, $y/D = 0.042$ ($S = fD/U_\infty$)

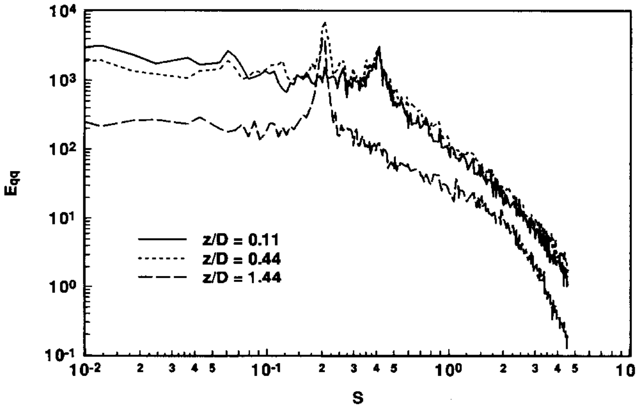

Figure 12 Power spectra of wall heat flux E_{qq} at different spanwise locations, $x/D = 5.2$ ($S = fD/U_\infty$)

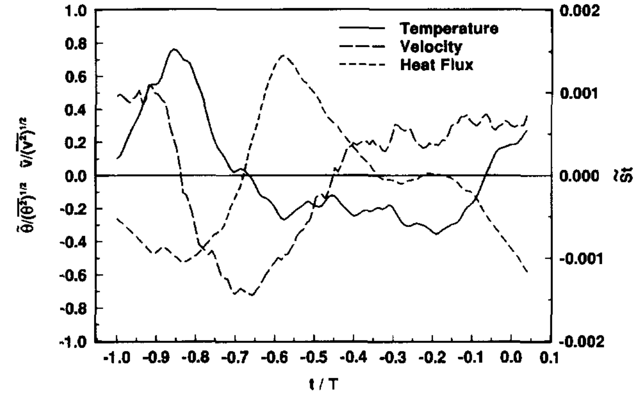

Figure 13 Ensemble-averaged temperature $\tilde{\theta}/\sqrt{\overline{\theta^2}}$, and velocity $\tilde{v}/\sqrt{\overline{v^2}}$, at $x/D=5.2$, $y/D=0.042$, $z/D=-0.44$, and ensemble-averaged wall heat flux, St at $x/D=5.2$, $z/D=0.44$

The peak-to-peak difference of the ensemble-averaged temperature is shown in Figure 14. These results indicate the strong role that unsteadiness plays in the transport process. The strongest effect is seen in the unsteady region, where the temperature difference shows a peak value of 1.5°C at $y/D = 0.022$ and $z/D = -1.22$. In the outer region, where the flow is approaching an undisturbed boundary layer, periodic unsteadiness has little effect on transport. In the wake region, the data show that the unsteady effect is still important close to the wall.

Ensemble-averaged wall heat flux at five different spanwise locations, $z/D = 0.11$, 0.22 (wake region), 0.44, 1.22, and 1.44, (unsteady region) are plotted in Figure 15. At $z/D = 0.11$, the ensemble-average heat flux is characterized by two peaks, near $\tau/T = -0.5$ and -0.1. This is consistent with the spectrum shown in Figure 12, which exhibited a peak at the first harmonic of the vortex shedding frequency, but no peak at the shedding frequency itself. At $z/D = 0.22$, both peaks are still evident, but the first peak is significantly stronger. The second peak is not observed in the unsteady region, but the first peak becomes broader. At $z/D = 1.22$, the largest fluctuations in wall heat flux were observed, consistent with the behavior of the ensemble-averaged temperature, which also reached a maximum near $z/D = 1.22$. It should be noted that the peak-to-peak variations in the ensemble averaged Stanton number at $z/D = 1.22$ were approximately 25% of the mean adiabatic Stanton number as measured by the thin-film sensors. Beyond that spanwise location, the fluctuations in wall heat flux decrease, as the effect of the unsteadiness becomes less important.

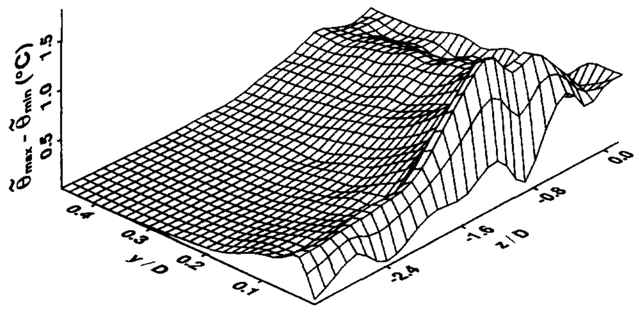

Figure 14 Peak-to-peak difference in ensemble-averaged mean temperature $\tilde{\theta}_{max} - \tilde{\theta}_{min}$

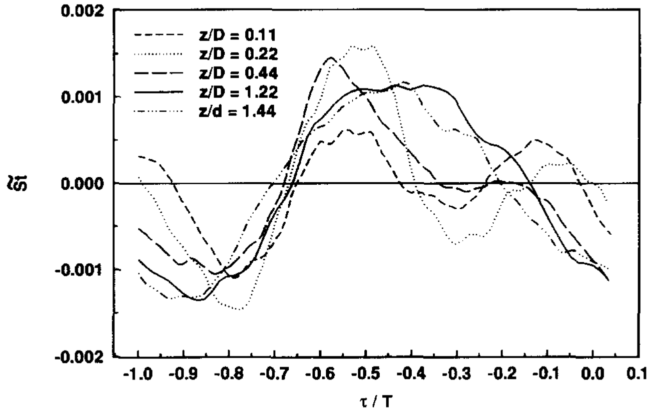

Figure 15 Ensemble-averaged wall heat flux, St at different spanwise locations, $x/D=5.2$

Figure 16 shows isocontours of the ensemble-averaged temperature (with the local mean values added) for three different phase times within a typical event cycle $\tau/T = -0.85$, -0.7, and -0.55. Below the contour plots are bar graphs that illustrate the behavior of the ensemble-averaged wall Stanton number at seven spanwise locations. These show the Stanton number at the specific phase time (dark bars) relative to the maximum and minimum values. At $\tau/T = -0.85$, the Stanton numbers are all at or near their minimum values, and the contour plot indicates that the thermal boundary layer is thickest. As phase-time progresses, the boundary layer thins, as a downwash carries low-temperature

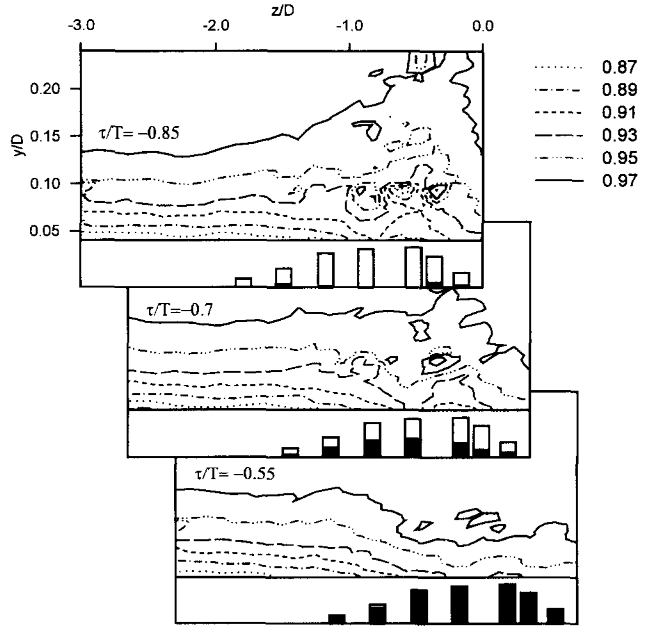

Figure 16 Isocontours of ensemble-averaged temperature, $(\tilde{\theta}+\bar{\theta}-T_{w,2d})/(T_\infty - T_{w,2d})$ at different phase times within event cycle, $\tau/T = -0.85$, -0.7, and -0.55; $x/D=5.2$; bars below contour plots represent ensemble-averaged wall Stanton numbers—open bars are maximum values, and filled bars represent the value at that particular phase

fluid toward the wall. At $\tau/T = -0.55$, corresponding to the phase of maximum Stanton number, the boundary layer has been thinned significantly. This further confirms that the the temporal variations in Stanton number were due to the thinning and thickening of the thermal boundary layer. The spanwise extent of the unsteadiness is also revealed, with almost no change in the temperature field outside of $z/D = -2.0$ and only a modest change directly behind the cylinder.

Uncertainties

The experimental uncertainties for the various quantities presented in this paper are *N*th-order uncertainties, calculated based on the single-sample methodology described by Moffat (1988). The *N*th-order uncertainty of a result is a measure of its overall uncertainty, accounting for all sources of fixed and random errors in the experiment as it was conducted. The *N*th-order uncertainties for nondimensional long-time mean velocity $\bar{u}/U_\infty$, temperature $(\bar{\theta} - T_{w,2d})/(T_\infty - T_{w,2d})$, and wall Stanton number $\mathrm{St}/\mathrm{St}_{2d}$ are ± 0.015, ± 0.05, and ± 0.12, respectively. The *N*th-order uncertainties for nondimensional ensemble-averaged mean vertical component of the velocity $\tilde{v}/(\overline{v^2})^{1/2}$ and temperature $\theta/(\overline{\theta^2})^{1/2}$ are ± 0.084 and ± 0.096, respectively.

Conclusions

The heat transport and wall heat transfer in a turbulent boundary layer downstream of a cylinder-wall junction has been investigated experimentally. The heat transfer effect of local periodic, large-scale unsteadiness, as a result of vortex shedding from the cylinder, is examined using a conditional data sampling and analysis technique that separated the large-scale periodic motion from the background turbulence. The results allowed the following conclusions to be made.

(1) The boundary-layer transport and wall heat transfer downstream of the cylinder-wall junction are strongly affected by the presence of large-scale, periodic unsteadiness arising from vortex shedding.

(2) The flow field is characterized by three different regions: (1) a wake region, where the unsteadiness is observed to have modest effect; (2) an unsteady region, where the strongest unsteadiness effect is found due to the vortex shedding; and (3) an outer region, where the flow is approaching 2-D boundary-layer behavior.

(3) Within the wake region, the vortex shedding from both sides of the cylinder may contribute to mixing enhancement and increased wall heat transfer. This is revealed by the power spectra, which show a peak at a frequency of twice the vortex-shedding frequency.

(4) Temperature, velocity, and wall heat transfer are characterized by large fluctuations in the unsteady region. The spectral peaks at the shedding frequency suggest that the periodic unsteadiness arises as a result of vortex shedding from the cylinder.

(5) Large-scale fluctuations of the time-resolved wall Stanton number are caused by the thinning and thickening of the near-wall thermal layer by the periodic fluctuations in the vertical component of the velocity. This is confirmed by the close correlation between the ensemble-averaged velocity, temperature, and wall heat flux. Ensemble-averaged wall Stanton number exhibits fluctuations up to 25% of the mean Stanton number.

Acknowledgments

Funding for this research was provided by the National Science Foundation under grant CTS-9211282. Thanks are also due to the contribution of Tina Swangard, who assisted with the design and testing of the surface sensors.

References

Baker, C. J. 1979. The laminar horseshoe vortex. *J. Fluid Mech.*, **95**, 347–367

Baker, C. J. 1980. The turbulent horseshoe vortex. *J. Wind Eng. Ind. Aerodynamics*, **6**, 9–23

Baughn, J. W., Takahashi, R. K., Hoffman, M. A. and McKillop, A. A. 1985. Local heat transfer measurements using an electrically heated gold-coated plastic sheet. *J. Heat Transfer*, **107**, 953–959

Fisher, E. M. and Eibeck, P. A. 1990. The influence of a horseshoe vortex on local convective heat transfer. *J. Heat Transfer*, **112**, 329–335

Goldstein, R. J. and Karni, J. 1984. The effect of a wall boundary layer on local mass transfer from a cylinder in crossflow. *J. Heat Transfer*, **106**, 260–267

Hunt, J. C. R., Abell, C. J., Peterka, J. A. and Woo, H. 1978. Kinematical studies of the flow around free or surface-mounted obstacles; Applying topology to flow visualization. *J. Fluid Mech.*, **86**, 179–200

Kays, W. M. and Crawford, M. E. 1993. *Convective Heat and Mass Transfer*, McGraw-Hill, New York, 267–270

Moffat, R. J. 1988. Describing uncertainty in experimental results. *Exp. Thermal Fluid Sci.*, **1**, 3–17

Norberg, C. 1994. An experimental investigation of the flow around a circular cylinder: Influence of aspect ratio. *J. Fluid Mech.*, **258**, 287–316

Oertel, H. Jr. 1990. Wakes behind blunt bodies. *Ann. Rev. Fluid Mech.*, **25**, 539–564

Pierce, F. J. and Harsh, M. D. 1988. The mean flow structure around and within a turbulent junction or horseshoe vortex—Part II. The separated and junction vortex flow. *J. Fluids Eng.*, **110**, 415–423

Praisner, T. J., Seal, C. V., Takmaz, L. and Smith, C. R. 1996. Spatial-temporal turbulent flow-field and heat transfer behavior in end-wall junctions. *Proc. Int. Turbulent Heat Transfer Conference*, San Diego, CA

Shabaka, I. M. M. A., Mehta, R. D. and Bradshaw, P. 1985. Longitudinal vortices embedded in turbulent boundary layers. *J. Fluid Mech.*, **155**, 37–57

Sparrow, E. M., Stahl, T. J. and Traub, P. 1984. Heat transfer adjacent to the attached end of a cylinder in crossflow. *Int. J. Heat Mass Transfer*, **27**, 233–242

Swisher, S. E., Diller, T. E. and Pierce, F. J. 1992. Time-resolved heat flux measurements in a turbulent junction. In *Topics in Heat Transfer*, HTD, Vol. 206-1, ASME, New York, 55–63

Tyszka, D. A., and Wroblewski, D. E. 1996. Heat transfer and fluid mechanics measurements in the turbulent endwall junction boundary layer downstream of a streamlined body. *J. Heat Transfer*, **118**, 485–488

Wroblewski, D. E. and Eibeck, P. A. 1992. Turbulent heat transfer in a boundary layer behind a junction of a streamlined cylinder and a wall. *J. Heat Transfer*, **114**, 840–849

Wroblewski, D. E. 1996. Effect on large-scale periodic unsteadiness on heat transport in the downstream region of a junction boundary layer. *Int. J. Heat Fluid Flow*, **17**, 3–11

Xie, Q. 1996. Periodic unsteady effects on turbulent boundary layer transport and heat transfer: An experimental investigation in a cylinder-wall junction flow. Ph.D. Thesis, Boston University, Department of Aerospace and Mechanical Engineering